DOI: 10.26599/FSHW.2026.9250923

Contents lists available at SciOpen

Food Science and Human Wellness

journal homepage: https://www.sciopen.com/journal/2097-0765

China Food Publishing Co.

Ketogenic diet mitigates sepsis-associated acute kidney injury in mice via reactivation of fatty acid oxidation: a multi-omics and mechanistic study

Siyao Zeng[1†], Zhipeng Yao[1†], Chumming Guan[1†], Yu Zhang[2†], Shanpeng Cui[1], Zhen Quan[1], Lianghe Wen[1], Junbo Zheng[1*], Yue Li[1*], Hongliang Wang[1*]

[1]*Department of Critical Care Medicine, Second Affiliated Hospital of Harbin Medical University, Heilongjiang Province, Harbin, 150086, China*

[2]*State Key Laboratory of Frigid Zone Cardiovascular Diseases, Department of Pharmacology, College of Pharmacy, Harbin Medical University, Harbin, China*

ABSTRACT: Sepsis-associated acute kidney injury (SA-AKI) is a severe complication of sepsis characterized by impaired fatty acid oxidation (FAO) and lipid accumulation in renal tissues, contributing to high mortality and morbidity. This study investigated the protective effects and underlying mechanisms of a ketogenic diet (KD)—high-fat, adequate protein, and low-carbohydrate intake—in a mouse model of SA-AKI induced by lipopolysaccharide (LPS). Male C57BL/6 mice were randomized into control, SA-AKI, and KD-treated groups. Results demonstrated that KD significantly ameliorated renal dysfunction, as indicated by reduced serum creatinine (Scr), blood urea nitrogen (BUN), kidney injury molecule-1 (KIM-1), neutrophil gelatinase-associated lipocalin (NGAL), and pro-inflammatory cytokines including interleukin-1β (IL-1β), interleukin-6 (IL-6), and tumor necrosis factor-α (TNF-α). Histological analysis revealed preservation of renal tubular architecture and reduced lipid accumulation in KD-treated mice. Integrated multi-omics analyses—untargeted proteomics, targeted proteomics via parallel reaction monitoring (PRM), untargeted metabolomics, and untargeted lipidomics—identified significant metabolic remodeling associated with KD treatment. Proteomic analyses showed KD reversed SA-AKI-induced dysregulation of key FAO enzymes, notably acyl-CoA thioesterase 2 (ACOT2) and acyl-CoA thioesterase 4 (ACOT4). Metabolomics highlighted changes in FAO intermediates such as acylcarnitines, while lipidomics revealed normalization of triglycerides, diglycerides, and various phospholipids. Integrated correlation analysis confirmed robust interactions among proteins, metabolites, and lipid species linked to FAO. Mechanistically, KD restored renal adenosine triphosphate (ATP) levels and enhanced citrate synthase activity and FAO capacity. Additionally, KD treatment markedly upregulated mRNA and protein expressions of peroxisome proliferator-activated receptor alpha (PPARα), peroxisome proliferator-activated receptor gamma coactivator 1-alpha (PGC1α), carnitine palmitoyltransferase 1A (CPT1A), carnitine palmitoyltransferase 2 (CPT2), and acyl-CoA oxidase 1 (ACOX1). Activation of the AMP-activated protein kinase (AMPK)–PGC1α–PPARα signaling pathway was further validated by Western blot and immunofluorescence analyses. These findings suggest that KD may mitigate SA-AKI by enhancing FAO and lipid homeostasis, supporting its potential as a therapeutic approach.

Keywords: Fatty acid oxidation, Ketogenic diet, Multi-omics, Sepsis-associated acute kidney injury

[†]Siyao Zeng, Zhipeng Yao, Chumming Guan and Yu Zhang contributed equally to this work.
***Corresponding author**
icuwanghongliang@163.com, liyuevickey@126.com, icuzhengjunbo@126.com

Received 1 August 2025
Received in revised from 7 September 2025
Accepted 24 September 2025

1. Introduction

Among critically ill patients with sepsis, one of the most frequent and severe types of organ dysfunction is acute kidney injury (AKI), commonly referred to as sepsis-associated acute kidney injury (SA-AKI) (1). A 2024 multicentre cohort study encompassing more than 4 000 critically ill adults reported an SA-AKI incidence of 62.3%, with severe stages nearly doubling in-hospital mortality relative to sepsis without AKI (2). The condition imposes substantial demands on intensive care resources, including extended intensive care unit (ICU) stays. In the long term, SA-AKI is associated with heightened risks of persistent renal dysfunction and multi-organ impairment, further complicating recovery trajectories and increasing healthcare burden (3-5). SA-AKI is managed with supportive care, including prompt infection control, aggressive fluid resuscitation, vasopressor support, and renal replacement therapy (RRT) in severe cases (1, 6). To date, no pharmacologic agent has proven effective in targeting the unique pathophysiology of SA-AKI, so interventions remain largely non-specific (1, 6). Moreover, life-sustaining therapies like RRT carry their own risks, as intradialytic hypotension and other hemodynamic instabilities can further compromise renal perfusion and hinder recovery (7).

Metabolic reprogramming refers to the adaptive alteration of cellular metabolic pathways in response to environmental stressors, enabling cells to meet shifting energy demands. In healthy states, renal proximal tubular epithelial cells (TECs) predominantly rely on fatty acid oxidation (FAO) as a key energy source. However, during sepsis, metabolic reprogramming in TECs may reprioritize cellular functions, leading to impaired FAO and reduced adenosine triphosphate (ATP) production (8). Accumulating evidence indicates that FAO is markedly suppressed in various forms of AKI, with mitochondrial FAO activity reduced by up to 40% under inflammatory conditions such as sepsis (9, 10). This suppression of FAO is increasingly recognized as a common pathogenic mechanism underlying SA-AKI (1, 9, 11). Following the onset of SA-AKI, reduced FAO in TECs leads to progressive lipid accumulation, which in turn exacerbates tubular and glomerular damage, accelerating the course of renal injury. Moreover, this lipid accumulation has been implicated in the development of tubulointerstitial fibrosis and glomerulosclerosis, further contributing to long-term kidney dysfunction (8, 12).

In renal tissues, AMP-activated protein kinase (AMPK) functions as an energy sensor and plays a critical role in maintaining cellular energy balance. When ATP is depleted, AMPK is activated and initiates energy-conserving pathways, including FAO, while simultaneously inhibiting energy-consuming processes such as protein synthesis, thereby restoring energy homeostasis (13). Its downstream target, peroxisome proliferator-activated receptor γ coactivator-1α (PGC1α), serves as a master regulator of mitochondrial biogenesis, promoting the expression of mitochondrial proteins and oxidative phosphorylation (OXPHOS) to provide ATP for cells (14). PGC1α further cooperates with peroxisome proliferator-activated receptor α (PPARα) to activate the expression of key FAO enzymes such as carnitine palmitoyltransferase 1 (CPT1) and acyl-CoA oxidase 1 (ACOX1), thereby enhancing mitochondrial FAO (15). This pathway sustains high levels of FAO in normal renal proximal TECs, providing continuous energy for reabsorptive activity and

representing an essential component of renal metabolic homeostasis (13, 16). Conversely, disruption of AMPK-PGC1α–PPARα signaling pathway impairs FAO, leading to intracellular lipid accumulation in TECs and exacerbation of renal injury (17). Given the central role of this pathway in sustaining renal FAO, interventions that enhance AMPK–PGC1α–PPARα signaling may hold therapeutic potential.

Emerging adjunctive approaches from traditional Chinese medicine (TCM) and the concept of "medicine–food homology" (MFH) are gaining attention (18). MFH recognizes that certain foods and herbs can serve as medicinal agents, and indeed many TCM-derived therapies (some officially dual-listed as food and medicine) exhibit anti-inflammatory and organ-protective activities (18). For example, bioactive compounds from TCM such as Rehmannia glutinosa have demonstrated nephroprotective effects in experimental AKI models, alongside broader anti-inflammatory, antioxidant, and immunomodulatory properties (19). These interventions are generally well-tolerated and suitable for long-term use, acting via multi-target mechanisms to modulate immune and inflammatory pathways with minimal systemic toxicity (18, 19). This evolving landscape of adjunctive therapies highlights a critical shift toward addressing the underlying pathobiology of SA-AKI, complementing supportive care with interventions that confer anti-inflammatory, metabolic, and nephroprotective benefits (18, 19). Compared with conventional supportive therapies, metabolic interventions such as the ketogenic diet (KD) may represent a novel strategy for alleviating SA-AKI. A nutritional pattern consisting of high fat, sufficient protein, and restricted carbohydrates facilitates a metabolic shift toward enhanced FAO and ketogenesis, commonly referred to as the KD (20, 21). By limiting carbohydrate intake without reducing protein, KD suppresses insulin secretion, thereby promoting FAO and ketogenesis (22). In renal tissues, upregulation of FAO through KD has been shown to attenuate fibrosis and protect against injury, suggesting potential therapeutic relevance in kidney diseases (23). Recent studies further confirm that KD enhances FAO both systemically and at the organ level (24).

Advances in multi-omics technologies have transformed the investigation of complex conditions such as SA-AKI, offering integrated insights into disease mechanisms through proteomic, metabolomic, and lipidomic profiling (25-27). In this study, we applied an integrative phenomics approach—combining untargeted proteomics, targeted proteomics via parallel reaction monitoring (PRM), untargeted metabolomics, and untargeted lipidomics—to explore the molecular effects of KD intervention in SA-AKI. This multi-layered strategy allowed for the systematic characterization of protein, metabolite, and lipid alterations in renal tissues, thereby capturing the metabolic remodeling associated with KD treatment. This study aimed to investigate the protective effect of a ketogenic diet against SA-AKI in mice, and to explore its underlying mechanism based on FAO remodeling, as revealed by integrated multi-omics analyses and validated through key protein expression. The findings provide mechanistic evidence supporting the ketogenic diet as a potential metabolic intervention strategy for SA-AKI.

2. Materials and methods

2.1 Animal model

Male C57BL/6 mice (6–8 weeks, 20–25 g; Charles River Laboratories) were acclimated for one week under specific pathogen-free (SPF) conditions before random assignment into control (C group), lipopolysaccharide (LPS)-induced SA-AKI (L group), and KD group (n = 6 each). Mice in the KD group were fed a ketogenic diet (Synergy Bio, China) for seven days, while those in the C and L groups were maintained on a standard chow diet. The Nutrient Composition Table is shown in Table S1. SA-AKI was induced by intraperitoneal injection of LPS (10 mg/kg, Sigma-Aldrich) dissolved in phosphate-buffered saline (PBS; VivaCell, China) in the L and KD groups, while control animals received PBS alone. All procedures complied with institutional ethical standards (Approval No. SYDW2024-127).

2.2 Sample collection

Twenty-four hours after LPS administration, all mice were anesthetized by intraperitoneal injection of tribromoethanol (brand name Avertin, Sigma-Aldrich), prepared according to established protocols. A stock solution was made by dissolving 1 g of 2,2,2-tribromoethanol in 1 ml of tert-amyl alcohol (2-methyl-2-butanol), then diluted to a working solution by adding 0.6 ml of this concentrate to 59.4 ml of sterile deionized water (yielding a 1.0% w/v solution). Each mouse (~20–25 g) received 0.4 ml intraperitoneally, equivalent to approximately 160–200 mg/kg of pure tribromoethanol, providing a surgical plane of anesthesia lasting about 20–30 minutes.

Under sterile conditions, peripheral blood was collected via retro-orbital venous puncture. Immediately following blood collection, mice were euthanized by cervical dislocation while still under deep anesthesia, as confirmed by the absence of reflex responses (e.g., toe-pinch). This procedure complies with the American Veterinary Medical Association (AVMA) guidelines, which recommend a humane physical method following chemical anesthesia to ensure rapid and painless death. Blood samples were left at room temperature for 30 minutes to clot, then centrifuged at 3000 r/min for 10 minutes at 4℃ to separate the serum for further biochemical testing. The right kidney was quickly frozen in liquid nitrogen and kept at –80℃ for molecular and biochemical analysis, while the left kidney was preserved in 10% neutral-buffered formalin for histopathological examination.

2.3 Tissue sectioning and staining procedures

Renal specimens were preserved in 10% neutral-buffered formalin, followed by stepwise dehydration in graded ethanol, paraffin embedding, and sectioning into 4 μm slices. Hematoxylin and eosin (H&E) staining was performed to evaluate histopathological changes. For periodic acid–Schiff (PAS) staining, sections were incubated with Schiff reagent for 10 minutes, washed under running water for 5 minutes, counterstained with Mayer's hematoxylin for 3 minutes, and rinsed again for another 5 minutes. All stained sections underwent alcohol dehydration, xylene clearing, and were finally mounted with coverslips for light microscopy observation.

To assess tubular injury, the following histological changes were considered indicators of damage: epithelial simplification, loss of brush border, apical blebbing, epithelial cell detachment, tubular dilation, and cast formation. For each sample, ten non-overlapping cortical or outer medullary fields were randomly

selected and examined at high magnification (×400). Two renal pathologists independently and blindly scored the images using a previously established semi-quantitative system: score 0, normal tubules without visible damage; score 1, ≤10% of tubules injured; score 2, 11%–25% injured; score 3, 26%–75% injured; score 4, >75% injured. The tubular injury score of each field was used for intergroup comparison.

Lipid accumulation in renal tissues was evaluated using Oil Red O staining on cryosectioned samples. Kidney sections (10 μm thickness) were fixed in 10% neutral-buffered formalin for 10 minutes and rinsed with distilled water. After fixation, the sections were stained with a freshly prepared Oil Red O solution for 10 minutes, briefly differentiated in 60% isopropanol, and washed again with distilled water. Nuclear staining was carried out using Harris hematoxylin for 1–2 minutes, followed by thorough rinsing under running water. Slides were then mounted with an aqueous medium and examined under a light microscope.

2.4 Assessment of renal function and inflammation

Renal function was assessed by quantifying serum creatinine (Scr) and blood urea nitrogen (BUN) levels with commercial colorimetric assay kits (Nanjing Jiancheng Bioengineering Institute, China), according to the manufacturer's guidelines.

Scr concentrations were determined using a creatininase–creatinase–sarcosine oxidase–peroxidase coupled enzymatic method. Serum samples (6 μL) were added to enzyme reagent A and incubated at 37 ℃ for 5 minutes. Enzyme reagent B was introduced, and the mixture was incubated at 37℃ for 5 minutes. Absorbance was measured at 546 nm with a microplate reader, and creatinine concentrations were determined by calculating the absorbance change using a calibration standard of 442 μmol/L.

BUN was measured using the urease–phenol–hypochlorite method. In brief, serum samples were incubated with urease-containing buffer at 37 ℃ for 10 minutes to hydrolyze urea into ammonium ions. Following the addition of phenol chromogenic reagent and alkaline hypochlorite, the mixture was incubated at 37℃ for 10 minutes. The developed blue color was measured at 640 nm, and BUN levels were determined by referencing a 10 mmol/L standard solution.

Quantitative real-time polymerase chain reaction (qPCR) was used to measure the expression levels of messenger ribonucleic acid (mRNA) for renal injury markers, including kidney injury molecule-1 (KIM-1) and neutrophil gelatinase-associated lipocalin (NGAL), as well as pro-inflammatory cytokines such as interleukin-1β (IL-1β), interleukin-6 (IL-6), and tumor necrosis factor-α (TNF-α). Total RNA was isolated from kidney tissues with RNA-Solv Reagent (Omega Bio-tek, USA) according to the manufacturer's protocol. Reverse transcription was carried out using 2 μg of total RNA and the TransScript First-Strand cDNA Synthesis SuperMix (Roche). qPCR was conducted using the TransStart Top Green qPCR SuperMix (TransGen Biotech, China). Gene expression was adjusted to glyceraldehyde-3-phosphate dehydrogenase (GAPDH) and determined via the comparative Ct method (2^–ΔΔCt). The primer sequences for amplification are provided in Supplemental Table S1 (RuiBiotech, China).

2.5 Immunohistochemistry

For immunohistochemical detection of KIM-1 and NGAL, paraffin-embedded renal sections (4 μm thickness) were first deparaffinized in xylene and rehydrated through graded ethanol. Antigen retrieval was performed using heat-induced epitope retrieval in citrate buffer (pH 6.0) at ~95 ℃ for 15 minutes to unmask fixation-masked epitopes. Endogenous peroxidase activity was quenched in 3% hydrogen peroxide for 10 minutes, followed by blocking with 5% normal goat serum for 30 minutes at room temperature. Sections were incubated overnight at 4 ℃ with primary antibodies against KIM-1 (1:200 dilution) and NGAL (1:300). After washing, slides were treated with biotin-conjugated secondary antibodies and a streptavidin–horseradish peroxidase complex, each for 30 minutes, then visualized using diaminobenzidine chromogen. Counterstaining was carried out with Mayer's hematoxylin for 1 minute. Finally, sections were dehydrated, cleared in xylene, mounted, and examined via light microscopy. Negative controls (without primary antibody) were included to confirm specificity. For semi-quantitative analysis, three non-overlapping renal sections were obtained from each animal (n = 6 per group). From each section, two randomly selected, non-overlapping cortical fields at ×200 magnification were analyzed, yielding six fields per animal (36 images per group). In each animal, these six images were analyzed and averaged to obtain a single representative value for statistical analysis (animal-level unit). All fields were selected by two independent investigators blinded to group allocation using a systematic random sampling approach to avoid selection bias. The positive staining area for KIM-1 and NGAL was measured using ImageJ software by thresholding the brown signal generated by 3,3′-diaminobenzidine (DAB) chromogenic reaction and expressed as a percentage of the total field area.

2.6 Measurement of β-hydroxybutyric acid

Renal β-hydroxybutyric acid (β-HB) concentrations in C, L, and KD groups were determined using liquid chromatography–mass spectrometry (LC-MS). Detailed protocols are provided in the Supplementary Methods 2.

2.7 Multi-omics analyses

Renal samples were subjected to untargeted proteomics, Targeted proteomics-parallel reaction monitoring (PRM), untargeted metabolomics, and untargeted lipidomics. Full experimental protocols including sample preparation, instrumentation, data acquisition, and bioinformatics analysis are provided in the Supplementary Methods 1.

2.8 Correlation analysis

To systematically investigate potential cross-omic interactions, an integrated multi-omics correlation analysis was performed incorporating PRM, metabolomics, and lipidomics datasets. Spearman correlation coefficients were calculated between selected differentially expressed proteins and all differentially expressed metabolites and lipids. Correlations with $|r| \geq 0.7$ and $P < 0.05$ were considered statistically significant and retained for downstream analysis. Correlation structures were visualized using two complementary methods: (1) a conventional heatmap annotated with Spearman r values to illustrate the strength and direction of

protein–small molecule associations; and (2) a circular network layout highlighting hierarchical relationships among molecular classes, excluding intra-class interactions. The network was constructed in Cytoscape (version 3.10.1), with protein nodes positioned at the center, metabolite nodes arranged in an intermediate circular layer, and lipid nodes distributed along the outermost circle. Node colors represented molecular categories—red for proteins, blue for metabolites, and green for lipids—while edge colors denoted correlation direction, with red indicating positive and blue indicating negative correlations.

2.9 Sankey diagram construction

A Sankey diagram was generated using the Plotly Python package (version 5.18.0) to visualize potential metabolic interactions among proteins, metabolites, and lipids. Key nodes were defined based on integrated multi-omics data, including PRM-validated proteins, differentially expressed metabolites, and significantly altered lipid species. Connections (links) between nodes were manually curated based on known biological relevance and established metabolic pathways. The width of each link was scaled proportionally to the relative abundance changes observed across experimental groups, thereby enabling visualization of putative metabolic flux alterations.

2.10 Joint pathway analysis

To investigate potential functional convergence between selected proteins and metabolites involved in fatty acid metabolism, Joint Pathway Analysis was performed using the MetaboAnalyst 5.0 platform. A representative subset of proteins and metabolites—screened from the PRM and metabolomics datasets based on biological relevance—was submitted to the "Joint Pathway Analysis" module, with the organism set to Mus musculus. Protein identifiers were provided as official gene symbols, and metabolite names were standardized according to Kyoto Encyclopedia of Genes and Genomes (KEGG) and Human Metabolome Database nomenclature. Pathway enrichment was conducted using the "combine queries" integration strategy and over-representation analysis (ORA). Significantly enriched pathways were visualized using KEGG metabolic maps to aid in biological interpretation and to highlight shared metabolic processes across omics layers.

2.11 Energy metabolism & lipid accumulation

Renal energy metabolism and lipid deposition were analyzed by assessing ATP levels, triglycerides (TG), glycerol, and non-esterified fatty acids (NEFA) using commercial colorimetric or luminescent assay kits (Nanjing Jiancheng Bioengineering Institute, China), as per the manufacturer's guidelines.

ATP concentrations were measured using a firefly luciferase-based chemiluminescence assay kit. Renal tissues were lysed in buffer (5–10 μL/mg tissue), centrifuged at 12,000 ×g for 5 minutes at 4℃, and the supernatants were analyzed in white 96-well plates. Luminescence was detected with a luminometer. ATP levels were adjusted for total protein and expressed as relative values, with results shown as fold changes in the L and KD groups compared to the C group.

TG levels were quantified using the glycerol-3-phosphate oxidase – phenol aminophenazone technique. Kidney tissues were homogenized in 0.9% saline (1:9, w/v), centrifuged, and 2.5 μL of supernatant was mixed with 250 μL of reaction reagent in a 96-well plate. After incubating at 37℃ for 10 minutes, absorbance was recorded at 500 nm. Results were normalized to protein concentration and reported as mmol/g.

Glycerol levels were determined using a colorimetric assay kit, which quantifies glycerol via enzymatic conversion to hydrogen peroxide and chromogenic dye. Each sample (10 μL) was combined with 190 μL of working solution in 96-well plates, and absorbance was recorded at 505 nm. Glycerol concentrations were determined using a standard curve and adjusted for total protein.

NEFA concentrations were determined using a two-step enzymatic procedure. Samples (4 μL) were incubated with reagent 1 followed by reagent 2 at 37℃, and the optical density was recorded at 546 nm before and after the second incubation. NEFA levels were derived from ΔA values and expressed as mmol/gprot.

2.12 Mitochondrial function & FAO capacity

Citrate synthase activity, a surrogate marker of mitochondrial content and function, was quantified with a commercial colorimetric assay kit (Nanjing Jiancheng Bioengineering Institute, China). Renal tissues were processed in extraction buffer at a ratio of 1:9 (g/mL), centrifuged at 10,000 r/min for 10 minutes at 4 ℃, and the supernatant was collected. The assay was performed in 96-well plates: reaction mixtures containing buffer, substrate, and chromogenic agent were pre-incubated at 37 ℃ for 3–5 minutes before adding 10 μL of sample. Absorbance was measured at 412 nm both at baseline (0 min) and after 15 min incubation. Citrate synthase activity was calculated using the change in absorbance over time and normalized to protein concentration.

FAO capacity was assessed using a colorimetric assay kit (Elabscience, China). Kidney tissue was lysed in 0.9% saline (1:9, g/mL), and the supernatant was collected after centrifugation at 10,000 ×g for 15 minutes at 4℃. The assay was conducted in 96-well plates following the manufacturer's instructions: 50 μL of the sample was mixed with substrate, cofactor, and chromogenic reagents, then incubated at 37℃ for 30 minutes. Absorbance was recorded at 450 nm using a microplate reader. FAO capacity was determined from a standard curve and adjusted for total protein content.

2.13 qPCR for FAO-related genes

To examine the transcriptional regulation of FAO, qPCR was performed to assess mRNA expression of key FAO-related genes, including, PGC1α, PPARα, carnitine palmitoyltransferase 1A (CPT1A), carnitine palmitoyltransferase 2 (CPT2), and ACOX1. RNA extraction, reverse transcription, and qPCR procedures were carried out as previously described. Primer sequences are listed in Supplementary Table S2.

2.14 Western blotting

Western blotting was performed to evaluate the protein expression of KIM-1, NGAL, AMPK, phosphorylated AMPK (P-AMPK), PGC1α, PPARα, CPT1A, CPT2, and ACOX1. Kidney tissues were lysed, and total proteins were extracted using standard lysis buffer. Equal amounts of protein were separated by 10% SDS-PAGE and transferred to polyvinylidene fluoride membranes. Membranes were blocked with 5% non-fat

milk and incubated overnight at 4 ℃ with primary antibodies targeting the proteins of interest and the internal control β-actin (beta-actin) (Proteintech Group, Wuhan, China). After incubation with horseradish peroxidase-conjugated secondary antibodies, the signals were visualized using enhanced chemiluminescence. Band intensities were quantified using ImageJ software (NIH, Bethesda, MD, USA) and normalized to β-actin.

2.15 Immunofluorescence

Immunofluorescence (IF) staining was performed to detect AMPK, P-AMPK, PGC1α, PPARα, CPT1A, CPT2, and ACOX1. Tissue sections were deparaffinized, subjected to antigen retrieval and permeabilization, and then washed three times with PBS (5 min each). After blocking with 5%–10% normal goat serum or bovine serum albumin (BSA) at room temperature for 1 hour, sections were incubated overnight at 4 ℃ with primary antibodies diluted in blocking solution. The next day, sections were washed three times with PBS and incubated with appropriate fluorophore-conjugated secondary antibodies for 1 hour at room temperature in the dark. Nuclei were counterstained with 4′,6-diamidino-2-phenylindole (DAPI), and slides were mounted with antifade medium and imaged using a fluorescence microscope. For semi-quantitative analysis, three non-overlapping renal sections were obtained from each animal (n = 6 per group). From each section, two randomly selected, non-overlapping cortical fields at ×400 magnification were imaged, yielding six images per animal (36 images per group). In each animal, these six images were analyzed and averaged to obtain a single representative value for statistical analysis (animal-level unit). Field selection and image analysis were performed by two independent investigators blinded to group allocation using a systematic random sampling approach to avoid selection bias. Images were acquired with identical exposure time, gain, and illumination settings across all groups and batches; background was subtracted uniformly. The mean fluorescence intensity of each target protein was quantified using ImageJ software by measuring integrated density within tubular regions of interest (ROIs) and normalized to DAPI-positive nuclei.

2.16 Statistical analyses

Statistical analyses were conducted using GraphPad Prism (version 10.0; GraphPad Software, La Jolla, CA, USA). Data are expressed as mean ± standard error of the mean (SEM). $*P < 0.05$, $**P < 0.01$, $***P < 0.001$ vs. L group. Comparisons between two groups were performed using unpaired Student's t-tests, and one-way analysis of variance (ANOVA) was used for comparisons among more than two groups.

3. Results

3.1 KD ameliorates SA-AKI

Histopathological analysis corroborated the renoprotective effects of KD in SA-AKI (Fig. 1A). H&E staining demonstrated pronounced tubular injury in the L group, evidenced by cellular edema, vacuolar degeneration and tubular lumen narrowing. In contrast, KD treatment markedly attenuated these pathological changes, with preservation of tubular architecture. Consistent with these findings, PAS staining revealed similar alterations, including cellular edema, vacuolar degeneration, and tubular lumen narrowing in the L

group, which were markedly alleviated in the KD group. Semi-quantitative analysis of PAS-stained sections further confirmed the severity of tubular injury, with significantly higher tubular injury scores in the L group compared to the C group, while KD treatment significantly reduced the injury score (Fig. 1C).

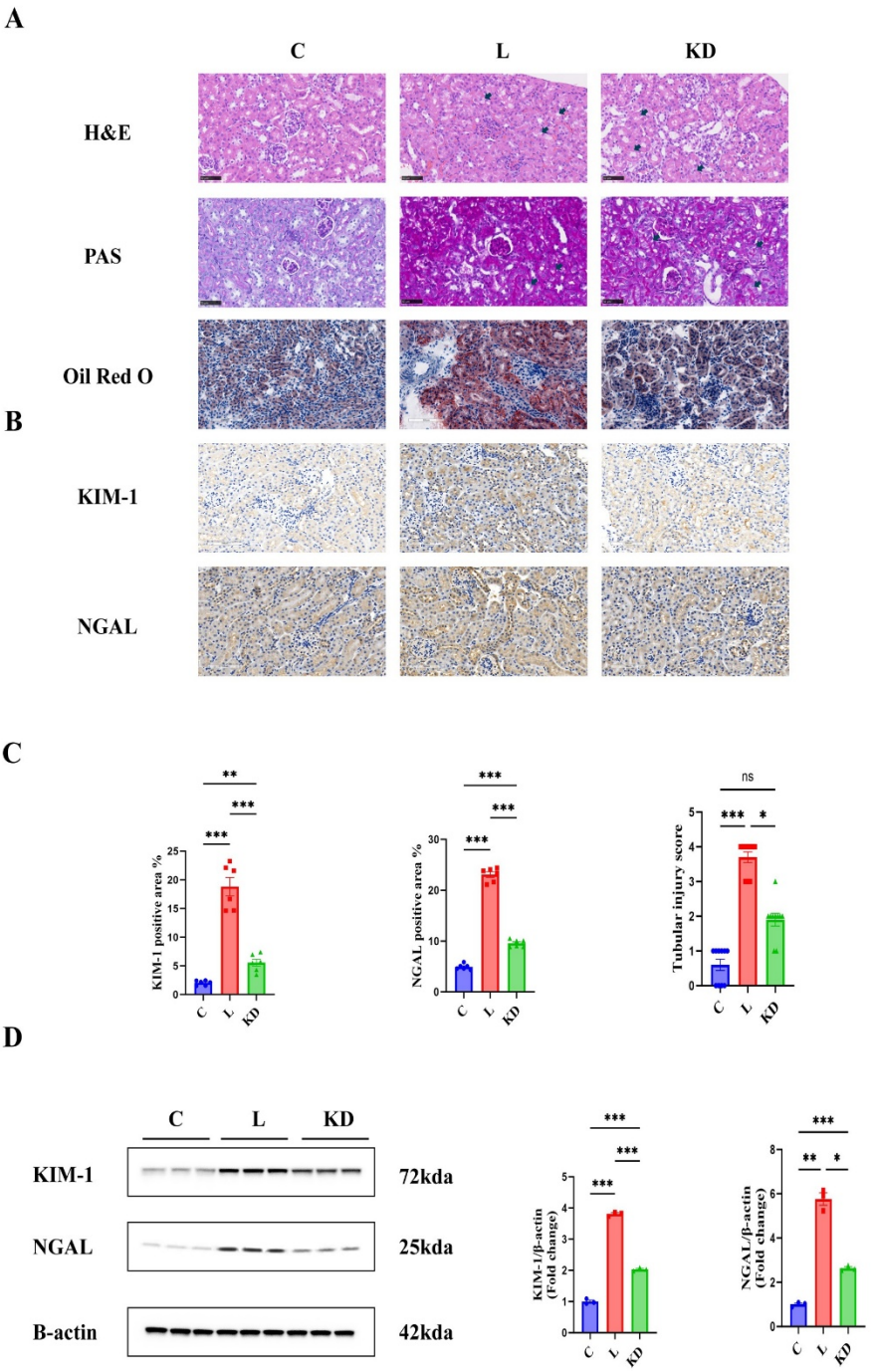

Fig. 1 A: Representative histological kidney sections stained with H&E, PAS, and Oil Red O from the C, L, and KD groups (original magnification ×20). The L group exhibited marked tubular injury characterized by cellular edema, vacuolar degeneration, and tubular lumen narrowing (indicated by black arrows), which were notably alleviated in the KD group.
B: Representative immunohistochemical staining for KIM-1 and NGAL in renal tissues (×200). Strong brown DAB signals were observed in the L group, indicating significant tubular epithelial injury, whereas KD treatment substantially reduced the expression of both markers.
C: Semi-quantitative analysis of immunohistochemistry and tubular injury. Semi-quantitative analysis of KIM-1 and NGAL positive staining areas was performed based on immunohistochemistry.
D: Western blot analysis of KIM-1 and NGAL. Representative blots and ImageJ quantification showing increased renal KIM-1 and NGAL protein expression in the L group compared with the C group, while KD intervention significantly reduced their levels. β-actin served as the control.

Compared with the C group, mice in the L group exhibited significant elevations in Scr, BUN, KIM-1, NGAL, as well as proinflammatory cytokines IL-1β, IL-6, and TNF-α, confirming successful establishment of the SA-AKI model (Fig. 2A-B). KD intervention markedly reduced the levels of these renal function indicators, inflammatory cytokines, and kidney injury markers relative to the L group, indicating that KD effectively attenuates LPS-induced renal dysfunction and inflammation in SA-AKI. Consistent with the qPCR results, immunohistochemical staining for KIM-1 and NGAL demonstrated strong positive signals in TECs of the L group, reflecting severe renal injury. In contrast, the KD group showed significantly decreased KIM-1 and NGAL staining intensity, indicating reduced epithelial damage and further confirming the protective effect of KD at the histological level (Fig. 1B-C). Furthermore, Western blot analysis and corresponding ImageJ semi-quantification revealed that protein expression levels of KIM-1 and NGAL were markedly increased in the L group compared with controls, whereas KD treatment significantly suppressed their expression (Fig. 1D), corroborating the histological and transcriptional findings.

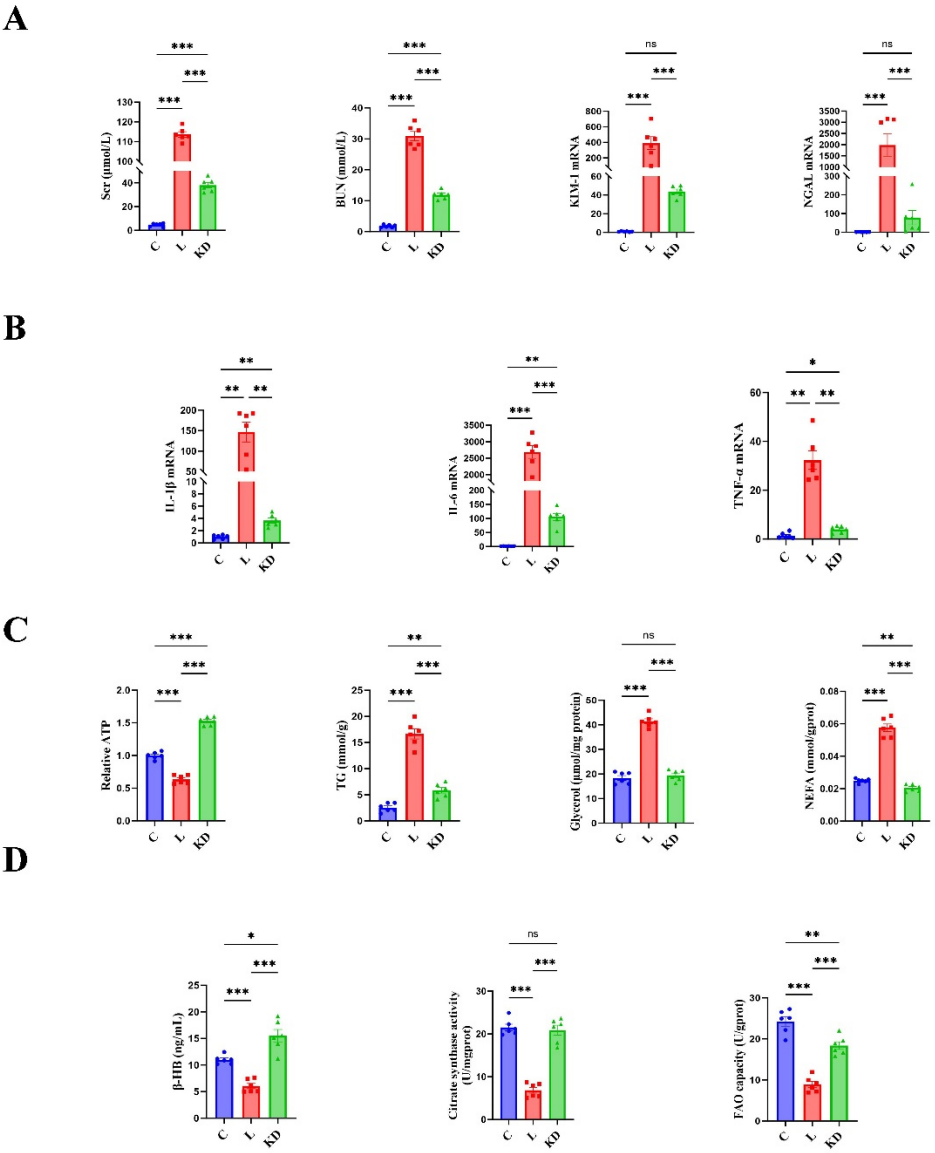

Fig. 2 A–B: Biochemical and inflammatory parameters in the C, L, and KD groups. The L group exhibited significant elevations in Scr, BUN, KIM-1 and NGAL, and pro-inflammatory cytokines IL-1β, IL-6, and TNF-α. These elevations were markedly attenuated by KD treatment. **C–D:** The L group also demonstrated evident metabolic dysregulation, characterized by elevated TG, glycerol, and NEFA, reduced ATP levels, decreased citrate synthase activity, diminished FAO capacity, and lower β-HB concentrations. KD intervention significantly restored these parameters.

3.2 Untargeted proteomics

A total of 8,076 proteins were identified, among which 7,884 were retained for downstream comparative analysis (Fig. S1A). Principal component analysis (PCA) revealed that one sample from the control group (C2) was an outlier, exhibiting lower reproducibility with Pearson's correlation coefficients (PCC) ranging from 0.7 to 0.8. Consequently, sample C2 was excluded from further analysis. The remaining samples demonstrated high reproducibility and consistent quality, as evidenced by PCA, PCC heatmaps, and boxplot distributions (Fig. S1B–D). Differentially expressed proteins (DEPs) were identified using a threshold of fold change >1.2 and $P < 0.05$. In the L/C comparison group, 1,693 proteins were upregulated and 1,405 were downregulated. In the KD/L comparison group, 308 proteins were upregulated and 170 downregulated (Fig. S1E). The distribution and expression patterns of these DEPs are illustrated by volcano plots and heatmaps (Fig. S1F–H). To further investigate the protein differences between the L/C and KD/L groups, we performed exploratory Venn diagram analysis to select 100 candidate proteins for subsequent PRM validation (Fig. S1I). The results showed that at a fold-change threshold of 1.245, 37 proteins were initially upregulated in the L/C group but reversed in the KD/L group, while 63 proteins were initially downregulated in the L/C group but reversed in the KD/L group. These 100 proteins were selected for targeted PRM validation.

3.3 PRM

Of the 100 candidate proteins selected for targeted validation, 85 were successfully quantified by PRM. Applying a significance threshold of fold change >1.2 and $P < 0.05$, volcano plots and Venn diagrams were generated to illustrate the expression dynamics across groups (Fig. S2A–C). Among these, 12 proteins that were initially upregulated in the L/C group were reversed in the KD/L group, while 19 proteins that were initially downregulated in the L/C group exhibited upregulation in the KD/L group. A heatmap displaying the expression profiles of these 31 proteins is presented in Fig. S2D. Quantitative comparisons between these 31 PRM-validated proteins and their corresponding expression trends in the untargeted proteomics dataset are shown in Fig. S2E–H. Notably, acyl-CoA thioesterase 2 (ACOT2) and acyl-CoA thioesterase 4 (ACOT4) were downregulated in the L/C group (0.66-fold and 0.43-fold, respectively) and reversed in the KD/L group (1.62-fold and 1.40-fold, respectively) based on untargeted proteomics. PRM validation revealed even more pronounced changes, with ACOT2 and ACOT4 reduced to 0.54-fold and 0.64-fold in the L/C group, and markedly increased to 3.06-fold and 2.61-fold, respectively, in the KD/L group. These findings confirm strong concordance between the PRM and untargeted proteomics results. A protein–protein interaction (PPI) network was constructed based on the intersection of differentially expressed proteins (fold change >1.2) identified in both the L/C and KD/L comparisons using untargeted and PRM proteomic data (Fig. S2I–J).

As shown in Fig. S3, Gene ontology (GO) enrichment analysis of the Biological Process (BP) category revealed significant enrichment in fatty acid metabolism pathways in both the L/C and KD/L groups, including the unsaturated and saturated monocarboxylic acid metabolic processes, as well as the very long-chain fatty acid catabolic process. In the Molecular Function (MF) category, the L/C group was enriched in acyl-CoA, coenzyme A (CoA), very long-chain acyl-CoA, and long-chain acyl-CoA hydrolase activities,

while the KD/L group additionally showed enrichment in medium-chain acyl-CoA hydrolase activity. KEGG pathway analysis further indicated that both groups were significantly associated with the fatty acid elongation pathway. The enrichment chord diagrams (Fig. S3) highlight that the GO and KEGG pathways enriched in both comparisons are functionally linked to ACOT2 and ACOT4, suggesting their central role in regulating fatty acid metabolism under septic conditions.

3.4 Untargeted metabolomics

A total of 645 metabolites were identified through untargeted metabolomics analysis. Principal component analysis (PCA), partial least squares discriminant analysis (PLS-DA), and orthogonal PLS-DA (OPLS-DA) demonstrated clear separation between the L/C and KD/L groups, indicating substantial metabolic alterations between the L and C groups and a marked impact of KD intervention on the L group (Fig. S4A). Using a threshold of fold change >1.5 and $P < 0.05$, volcano plot analysis (Fig. S4B) identified 192 upregulated and 121 downregulated metabolites in the L/C group, and 33 upregulated and 304 downregulated metabolites in the KD/L group. Heatmaps depicting metabolite abundance patterns are presented in Fig. S5–S6. Venn diagram analysis (Fig. S4C) revealed that 24 metabolites upregulated in the L/C group were reversed in the KD/L group, while 3 metabolites that were downregulated in the L/C group were also reversed following KD intervention (Table S3). Notably, several metabolites involved in the oxidation of long-chain fatty acids were identified, including hexanoylglycine, decadienedioic acid, 2-ethylpropanedioylc arnitine, acylcarnitine C6:1,OH, and O-butanoylcarnitine (19–21). Among these, hexanoylglycine was the only metabolite with a variable importance in projection (VIP) score <1 (0.98151) in the L/C comparison, while all others exceeded this threshold, indicating robust metabolic differences associated with FAO.

3.5 Untargeted lipidomics

A total of 546 lipids were identified in the untargeted lipidomics analysis. PCA, PLS-DA, and OPLS-DA revealed clear separation between the L/C and KD/L groups, indicating substantial lipidomic alterations between the L and C groups and a pronounced modulatory effect of KD intervention on lipid profiles (Fig. S7A). Based on a threshold of fold change >1.5 and $P < 0.05$, volcano plot analysis identified 127 upregulated and 28 downregulated lipids in the L/C group, whereas 92 lipids were upregulated and 175 were downregulated in the KD/L group (Fig. S7B). Heatmaps illustrating lipid abundance differences are presented in Fig. S8–S9. Venn diagram analysis (Fig. S7C) revealed that 66 lipids upregulated in the L/C group were reversed in the KD/L group, while 10 lipids downregulated in the L/C group also showed reversal following KD intervention (Table S4). Among the 66 reversed lipids, 35 were triglycerides (TG), 10 diglycerides (DG), and 8 sphingomyelins (SM), along with several phospholipids including phosphatidylethanolamines (PE), lysophosphatidylethanolamines (LPE), phosphatidylglycerols (PG), phosphatidylinositols (PI), bis(monoacylglycerol)phosphate (BMP), carnitines (CAR), cardiolipins (CL), and phosphatidylserines (PS). Of the 10 downregulated lipids reversed in the KD/L group, 3 were PI, 2 SM, and 1 each of TG, CL, PG, PS,

and sulfatide (SL). The vast majority of differentially expressed lipids had VIP scores ≥1, indicating strong discriminatory power and significant group differences.

3.6 Correlation network analysis

A Spearman correlation heatmap was first generated to illustrate the strength and direction of associations between selected differentially expressed proteins and small molecules (Fig. 3A). This analysis revealed that ACOT2 and ACOT4 were strongly positively correlated ($r \geq 0.7$) with several FAO-related metabolites, including acylcarnitine C6:1,OH, O-butanoylcarnitine, and 2-ethylpropanedioylcarnitine, as well as with multiple lipid species such as TG, DG, and phospholipids. To further visualize the topological structure of these molecular interactions, a circular multi-layered interaction network was constructed (Fig. 3B). In this network, central nodes (red) represent ACOT2 and ACOT4—key regulators of mitochondrial and peroxisomal FAO. The intermediate layer (blue) comprises five significantly altered metabolites associated with lipid metabolism, while the outer layer (green) includes TGs, DGs, SMs, and other lipid species that exhibited significant correlations with either proteins or metabolites. Edge colors denote the direction of correlation (red for positive, blue for negative). ACOT2 and ACOT4 demonstrated consistent correlation patterns across both visualizations, supporting their coordinated role in regulating FAO and lipid metabolism. Collectively, these integrated analyses highlight potential phenotypic associations among FAO-related proteins, lipid metabolites, and lipid species in the context of SA-AKI. The observed correlation patterns may reflect KD-associated modulation of renal lipid metabolism and suggest a role for enhanced FAO in the phenotypic response to dietary intervention.

3.7 Sankey diagram of ACOT2/4–metabolite–lipid interactions

The Sankey diagram (Fig. 3C) illustrated the phenotypic associations linking key FAO-related enzymes ACOT2 and ACOT4 to intermediate metabolites, which in turn correlated with differentially regulated lipid species, including TG, DG, SM, PE, and PI. This visualization highlights the distinct yet overlapping patterns of association involving ACOT2 and ACOT4, suggesting potential contributions of these enzymes to lipid metabolic remodeling in SA-AKI under KD intervention.

3.8 Joint pathway analysis

The joint pathway analysis integrating ACOT2/ACOT4 and five FAO-associated metabolites revealed enrichment in the fatty acid elongation pathway (Fig. 3D). The involved metabolites—such as hexanoylglycine and O-butanoylcarnitine—are typically associated with intermediate steps in fatty acid metabolism and may reflect alterations in medium-chain fatty acyl-CoA processing. Their localization within the elongation pathway suggests a potential accumulation of intermediate metabolites, possibly indicative of metabolic dysregulation in SA-AKI. These observations are consistent with a KD-associated shift toward normalization of FAO-related metabolic pathways, as reflected by the multi-omics phenotypic landscape.

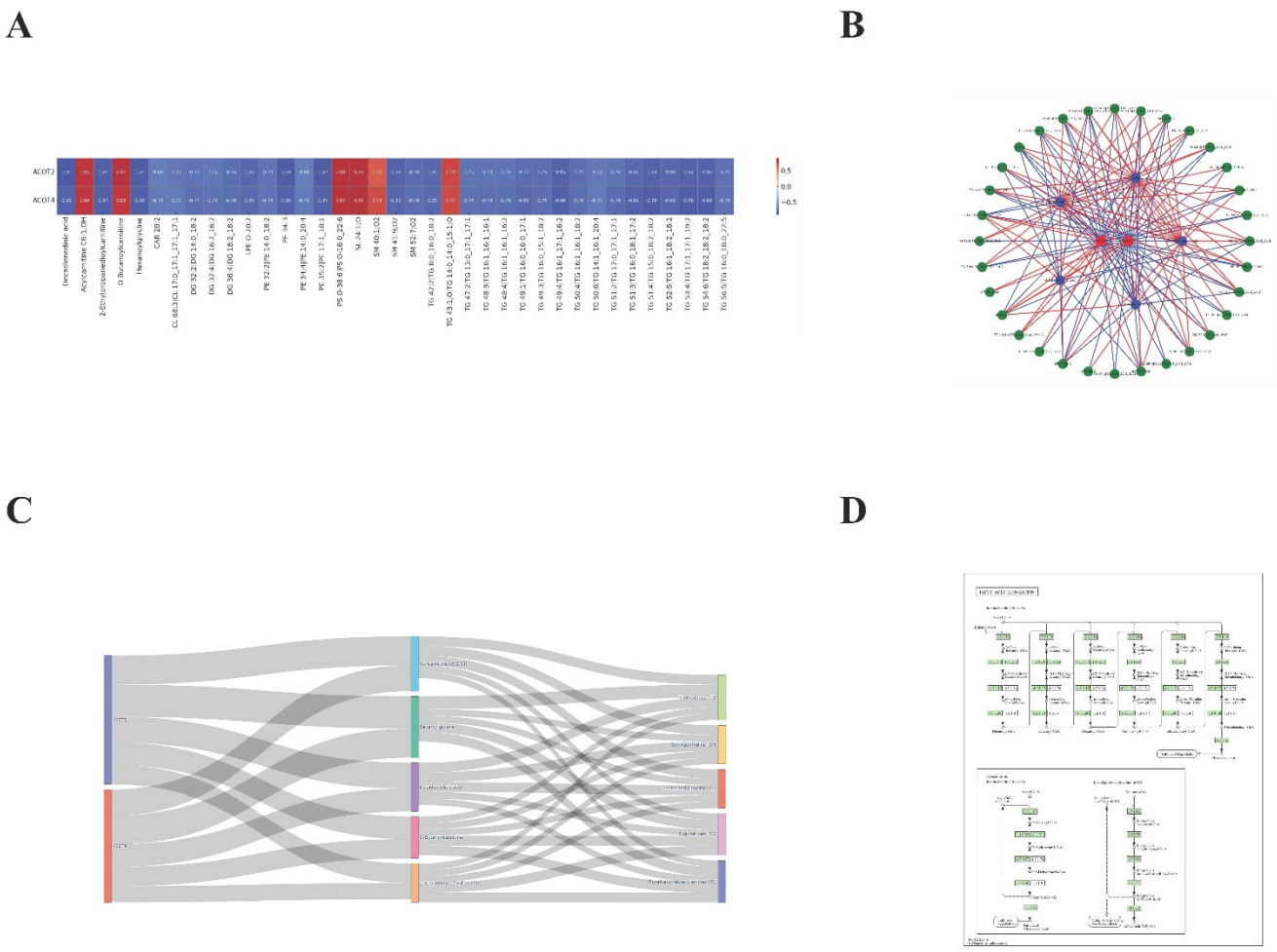

Fig. 3 A: Multi-omics correlation analysis among proteins, metabolites, and lipids. Spearman correlation heatmap showing significant associations ($|r| \geq 0.7$, $P < 0.05$) between selected proteins (ACOT2, ACOT4) and differential metabolites and lipid species. Color intensity reflects the strength and direction of correlation (red: positive; blue: negative), with numerical values indicating Spearman coefficients.
B: Circular protein–metabolite–lipid interaction network constructed based on the same significant correlations. Red nodes represent proteins, blue nodes represent metabolites, and green nodes represent lipids. Edges denote pairwise correlations (red: positive; blue: negative). The network layout emphasizes a hierarchical organization, with proteins placed at the center, metabolites in the intermediate layer, and lipids in the outermost layer. Only statistically significant associations are shown, highlighting potential regulatory hubs and coordinated metabolic responses involved in FAO reprogramming during SA-AKI.
C: Sankey diagram illustrating the metabolic connections between ACOT2/ACOT4, key intermediate metabolites, and lipid species.
D: KEGG pathway map of fatty acid elongation enriched by joint analysis of ACOT2/ACOT4 and five FAO-related metabolites. E: Schematic depiction of how KD reactivates FAO through ACOT2/4 and reshapes metabolite-lipid profiles in SA-AKI, as revealed by multi-omics integration.

3.9 KD restores energy metabolism and improves lipid metabolic balance

In the L group, renal ATP levels were significantly decreased, while TG content was markedly elevated, reflecting impaired energy production and disrupted lipid utilization. Glycerol and NEFA levels were notably higher in the L group, indicating increased lipolysis but insufficient subsequent oxidation, reflecting metabolic limitations. KD group markedly reversed these changes: ATP production was restored, and tissue levels of TG, glycerol, and NEFA were significantly reduced, suggesting recovery of mitochondrial energy output and improved lipid handling (Fig. 2C). These biochemical findings were corroborated by Oil Red O staining, which revealed extensive lipid droplet accumulation in the L group and substantial reduction following KD

administration, indicating attenuated lipid overload and enhanced fatty acid clearance in renal tissues (Fig. 1A). In addition, renal β-HB levels were markedly decreased in the L group compared with controls, while KD intervention significantly increased β-HB concentrations, indicating enhanced ketone body availability in renal tissues (Fig. 2D).

3.10 KD enhances FAO and mitochondrial function

Markers of mitochondrial function and FAO were assessed to further explore KD's mechanism of action. Citrate synthase activity, a surrogate marker of mitochondrial content and functional capacity, was significantly reduced in the L group but restored following KD intervention. Similarly, FAO capacity was markedly suppressed in the L group but significantly improved with KD treatment, indicating reactivation of renal FAO pathways and amelioration of metabolic dysfunction during SA-AKI (Fig. 2D).

3.11 KD enhances mRNA expression of FAO-related genes

Compared to the C group, the L group exhibited a marked decrease in the mRNA expression of all five genes (PPARα, PGC1α, CPT1A, CPT2, and ACOX1), reflecting suppression of mitochondrial lipid metabolism during SA-AKI. These reductions were significantly reversed by KD treatment. In particular, PPARα and PGC1α, two core transcriptional regulators of FAO, were notably upregulated, while the expression of CPT1A, CPT2, and ACOX1 was restored to levels comparable to controls (Fig. 4A). These results indicate that KD reactivates FAO at the transcriptional level.

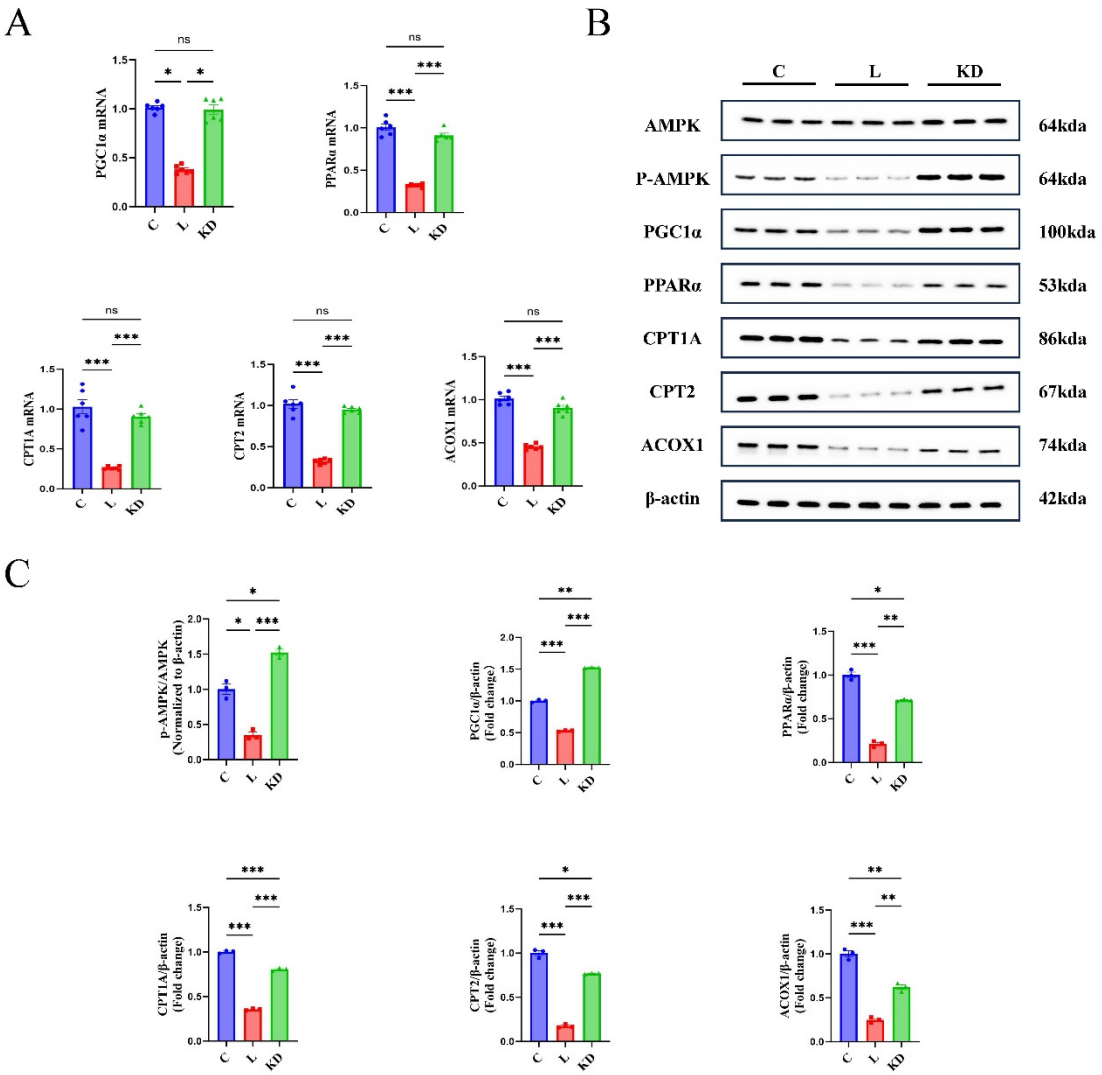

Fig. 4A: qPCR analysis of FAO-related genes (PPARα, PGC1α, CPT1A, CPT2, and ACOX1) in renal tissues from the C, L, and KD groups. The L group showed a significant reduction in mRNA expression of all five genes, indicating suppressed mitochondrial lipid metabolism during SA-AKI. KD treatment markedly restored their expression.
B: Representative Western blot images showing the expression levels of P-AMPK, AMPK, PGC1α, PPARα, CPT1A, CPT2, and ACOX1 in the C, L, and KD groups. Compared with the control, the L group exhibited decreased AMPK activation and reduced expression of FAO-related proteins, which were substantially reversed by KD intervention.
C: Densitometric quantification of protein expression normalized to β-actin. The L group showed a significant decrease in the P-AMPK/AMPK ratio and in the levels of PGC1α, PPARα, CPT1A, CPT2, and ACOX1. KD treatment significantly increased the expression of these proteins, indicating restored FAO pathway activity.

3.12 KD restores the AMPK–PGC1α–PPARα signaling pathway and upregulates FAO-related enzymes

Compared to the C group, the L group showed a significant reduction in the P-AMPK/AMPK ratio, indicating suppressed AMPK activation under septic stress. This was accompanied by decreased expression of PGC1α and PPARα, along with a marked downregulation of key FAO enzymes—CPT1A, CPT2, and ACOX1—reflecting impaired lipid oxidation in the kidneys. KD treatment effectively reversed these changes. The P-AMPK/AMPK ratio was significantly elevated, suggesting restored AMPK signaling, while PGC1α and PPARα were upregulated, supporting enhanced translational regulation of FAO. Additionally, expression levels of CPT1A, CPT2, and ACOX1 were substantially increased in the KD group relative to the L group, indicating recovery of FAO enzymatic activity (Fig. 4B-C). IF analysis further corroborated these findings: KD restored the expression and localization of P-AMPK, PGC1α, PPARα, CPT1A, CPT2, and ACOX1 in

renal tubular epithelial cells, which were markedly diminished in the L group (Fig. 5). These spatial data provide visual confirmation of KD-induced reactivation of the AMPK–PGC1α–PPARα signaling pathway and its downstream FAO components in kidney tissues.

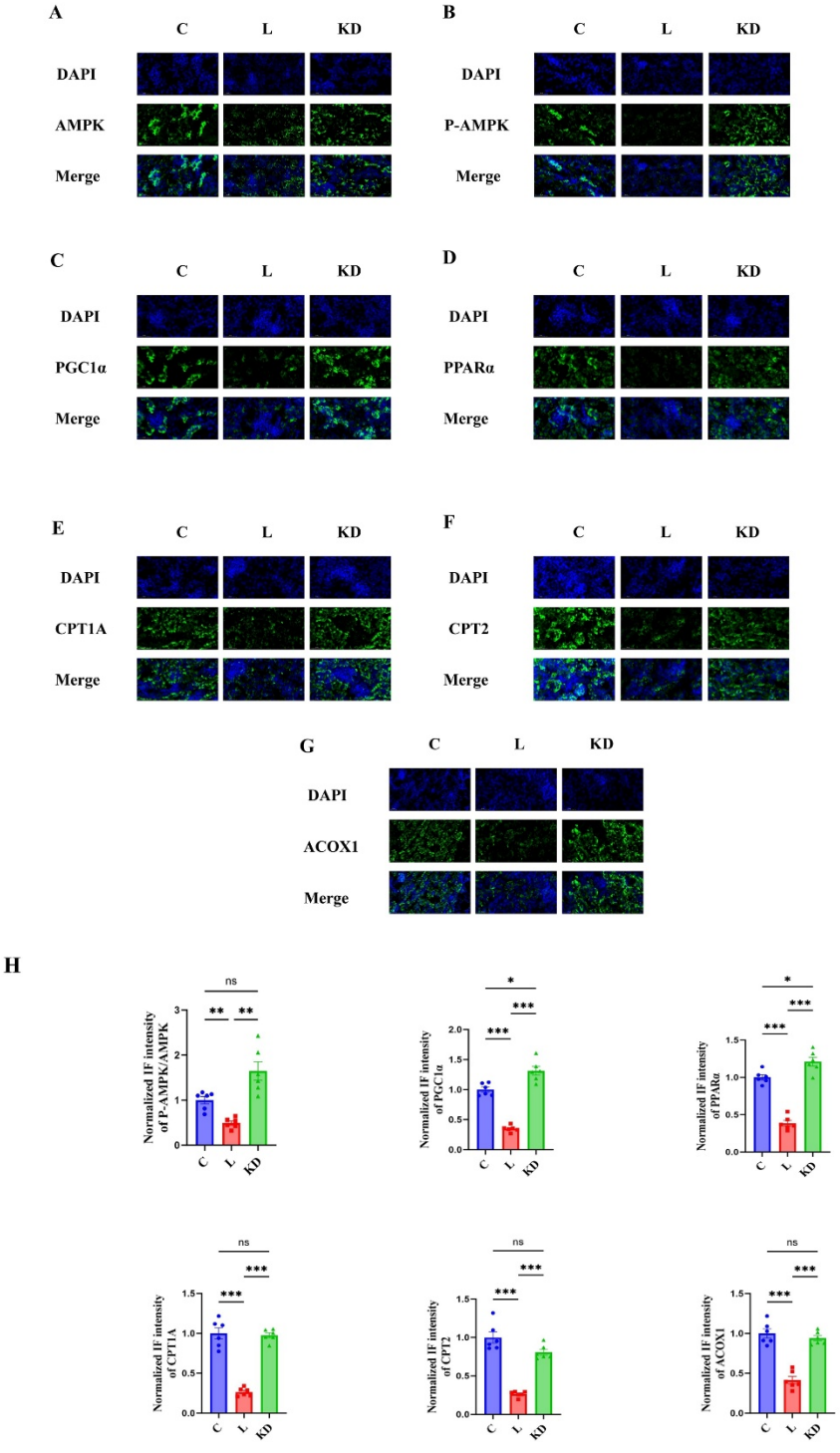

Fig. 5A–G: Representative IF images showing the expression and localization of AMPK, P-AMPK, PGC1α, PPARα, CPT1A, CPT2, and ACOX1 in renal tissues from the C, L, and KD groups (×400). DAPI (blue) indicates nuclear staining. The L group showed markedly reduced fluorescence intensity for P-AMPK, PGC1α, PPARα, and key FAO-related enzymes (CPT1A, CPT2, and ACOX1), indicating suppressed AMPK activation and impaired FAO during SA-AKI. KD treatment restored the expression of these proteins, with strong signals localized primarily in renal TECs.
H: Semi-quantitative analysis of immunofluorescence intensity based on six images per group, normalized to DAPI-positive nuclei. The L group exhibited significant reductions in P-AMPK, PGC1α, PPARα, CPT1A, CPT2, and ACOX1 fluorescence compared to controls, while KD intervention significantly increased their expression levels, confirming reactivation of the AMPK–PGC1α–PPARα signaling pathway and FAO-related protein restoration in kidney tissues.

4. Discussion

In the SA-AKI model, KD administration led to a marked reshaping of the renal phenotypic landscape, spanning molecular, biochemical, and histological domains. Histological assessments (H&E, PAS, and Oil Red O staining) demonstrated that KD alleviated tubular injury, preserved brush border integrity, and reduced lipid accumulation. Biochemically, KD-treated mice exhibited significantly lower levels of BUN, Scr, KIM-1, and NGAL, indicating improved renal function and reduced epithelial damage. Concurrently, renal metabolic markers—including ATP content, glycerol, TG, NEFA, and citrate synthase activity—were favorably modulated, reflecting a shift toward restored FAO. At the molecular level, multi-omics profiling revealed consistent FAO-related remodeling: proteomics showed upregulation of ACOT2 and ACOT4, key mitochondrial and peroxisomal enzymes regulating acyl-CoA turnover; metabolomics identified altered levels of key FAO intermediates such as acylcarnitines; lipidomics further revealed coordinated changes in TG, DG, and glycerophospholipids (28). These omics-based findings were further substantiated by transcriptional and translational validation. qPCR analyses confirmed that KD significantly upregulated the mRNA expression of pivotal FAO-related genes, including PGC1α, PPARα, CPT1A, CPT2, and ACOX1, which were notably downregulated under septic stress. Western blot results corroborated these changes at the protein level, showing that KD restored the P-AMPK/AMPK ratio and increased expression of downstream FAO effectors (PGC1α, PPARα, CPT1A, CPT2, ACOX1). Furthermore, immunofluorescence provided additional spatial evidence, demonstrating enhanced expression and localization of key FAO proteins in renal TECs following KD treatment. This multi-tiered validation strategy strengthens the mechanistic interpretation of how KD modulates FAO pathways to exert renal protective effects in SA-AKI. It is worth noting that among the canonical FAO regulators, only CPT2 was detected in our untargeted proteomics dataset. CPT2 expression was significantly elevated in the KD group compared to the L group, whereas its reduction in the L group relative to the control was not statistically significant. The lack of detection of other key FAO proteins (PPARα, PGC1α, CPT1A, ACOX1) likely reflects their relatively low abundance or tissue-specific expression, as well as the technical depth limits of untargeted proteomics approaches. This limitation underscores the value of complementary targeted validation. Our qPCR and Western blot analyses successfully confirmed the upregulation of all five classical FAO components in the KD group, thereby reinforcing the notion that KD reactivates FAO pathways. Together, this combination of unbiased discovery and targeted confirmation enhances the interpretability and robustness of our findings. Taken together, these findings indicate that KD induces a robust metabolic reprogramming in SA-AKI, primarily characterized by reactivation of the AMPK–PGC1α–PPARα signaling pathway and restoration of FAO activity, thereby ameliorating energy deficits and lipid toxicity in injured renal tissues.

Acyl-CoA thioesterases (ACOTs) catalyze the hydrolysis of fatty acyl-CoA into NEFA and free CoA, and are considered critical switches in regulating the rate of FAO (28). Specifically, ACOT2 is localized to the mitochondrial matrix, where it selectively hydrolyzes long-chain acyl-CoAs. Its overexpression prevents the intramitochondrial accumulation of acyl-CoA and simultaneously replenishes free CoA, thereby sustaining

high-flux β-oxidation (28). In the present study, KD restored renal ACOT2 expression, which may enhance mitochondrial CoA availability, alleviate acyl-CoA accumulation, and promote continuous FAO-derived energy production (28). ACOT4, in contrast, is mainly localized to renal peroxisomes, where it hydrolyzes medium- and short-chain dicarboxylic acyl-CoAs and recycles CoA (28). Upregulation of ACOT4 by KD may enhance the hydrolysis of medium- and short-chain dicarboxylic acyl-CoAs within peroxisomes, thereby facilitating more efficient metabolic coupling with mitochondrial oxidation and preventing CoA depletion in peroxisomes (28). Integrated multi-omics analyses revealed that changes in ACOT2/4 expression were significantly correlated with several FAO intermediates (e.g., acylcarnitine C6:1,OH) as well as TG, DG, and phospholipids, forming a metabolic network centered on ACOT2/4. These findings provide systems-level evidence that KD activates the ACOT2/4-mediated de-CoA-tion pathway, relieving a rate-limiting bottleneck in FAO and restoring tubular energy homeostasis.

Under normal conditions, TECs rely heavily on FAO as a primary energy source (29). In AKI, this metabolic preference is disrupted: there is a well-documented shift from FAO toward increased glycolysis (a "Warburg-like" reprogramming) (29). This phenomenon is especially pronounced in SA-AKI, where inflammatory and hypoxic stress suppress oxidative metabolism despite preserved renal blood flow (29). The result is impaired mitochondrial FAO with accumulation of lipids in injured TECs, contributing to energy deficits and cellular dysfunction (29). Loss of FAO is now recognized as a key driver of tubular injury and maladaptive repair. AKI kidneys show upregulation of CD36 (a fatty acid transporter), which promotes fatty acid uptake and lipotoxicity; transgenic mice overexpressing CD36 in tubules develop worse injury and fibrosis (29). Conversely, diminished expression of FAO enzymes correlates with worse outcomes – for example, lower CPT1A/ CPT2 levels in human kidneys associate with reduced glomerular filtration and higher circulating acylcarnitines (reflecting impaired FAO) (29). Functionally, inhibiting FAO exacerbates injury: treatment with the CPT1 inhibitor etomoxir was shown to suppress ATP production and trigger tubular cell dedifferentiation/apoptosis (29). On the other hand, boosting FAO can be protective. In experimental AKI, tubule-specific overexpression of CPT1A preserved mitochondrial integrity, reduced inflammation, and prevented fibrosis (29). These findings underscore that sustaining or restoring FAO in stressed tubules is crucial to mitigate AKI severity and subsequent fibrotic progression.

Consistent with prior studies, sepsis suppresses PPARα signaling and FAO: Feingold et al. reported that LPS administration reduces renal FAO by ~40%, accompanied by downregulation of CPT1 and ACOX1, along with marked decreases in PPARα and its coactivator PGC1α (30). This acute suppression of the PPARα–PGC1α signaling pathway in septic conditions halts the transcription of FAO genes, limiting FAO capacity and leading to lipid accumulation and energy deficiency in TECs (30). Correspondingly, PPARα deficiency exacerbates SA-AKI – PPARα-knockout mice exhibit worse kidney injury with reduced FAO and heightened inflammation, and septic patients with transcriptomic suppression of PPARα pathways have higher incidence of severe AKI (31). By contrast, interventions that preserve the AMPK–PGC1α–PPARα signaling pathway are renoprotective. Activation of AMPK stimulates PGC1α, which in turn co-activates

PPARα to induce FAO genes, including CPT1A/CPT2 and ACOX1, critical for FAO (23, 30). Pharmacological activation of AMPK during sepsis (using metformin) has been shown to improve survival and attenuate AKI, whereas AMPK inhibition worsens outcomes, reflecting the benefit of sustaining mitochondrial FAO (32). AMPK is a master energy sensor that directly promotes FAO and also enhances PGC1α activity; PGC1α in turn co-activates PPARα to induce transcription of FAO enzymes (e.g., CPT1A, CPT2, ACOX1) critical for fatty acid catabolism (30, 32). Thus, preserving the AMPK–PGC1α–PPARα signaling pathway helps maintain fatty acid utilization and ATP generation in stressed TECs, conferring renoprotection. Consistent with our results, a recent study in a murine renal fibrosis model demonstrated that a KD significantly upregulated CPT1A and ACOX1 expression with a concomitant increase in FAO, and notably, the renoprotective effect of KD was abolished by the CPT1 inhibitor etomoxir (23). These findings highlight that metabolic interventions can improve kidney outcomes by augmenting FAO through the AMPK–PGC1α–PPARα signaling pathway.

KD – a high-fat, low-carbohydrate diet that raises circulating ketone bodies – directly impacts renal energy metabolism. By shifting the primary fuel from glucose to fatty acids and ketones, KD can re-engage oxidative pathways in renal cells that are suppressed during AKI (33, 34). Emerging evidence indicates that ketosis has protective effects on the stressed kidney (33, 34). Importantly, while extreme ketoacidosis is harmful, modest elevations of ketone bodies (within physiologic ranges achievable by diet) appear to support renal cells during injury (35). Ketone bodies (β-hydroxybutyrate, acetoacetate) are efficiently reabsorbed and oxidized by proximal tubules as alternate fuels (35). Experimentally, boosting ketone availability has been shown to preserve ATP levels and mitigate injury in AKI models (35). For example, β-HB, the principal ketone, can protect kidneys via both metabolic and signaling mechanisms. β-HB not only serves as an energy substrate, but also modulates inflammation and gene expression. Tajima et al. (2019) reported that exogenous β-HB restored histone acetylation of the FOXO3 promoter in injured tubules, thereby enhancing antioxidant defenses and suppressing pyroptotic cell death (35). Consistently, a recent study in a murine SA-AKI model found that β-HB administration prior to endotoxin exposure significantly ameliorated SA-AKI, reducing tubular apoptosis and inflammatory cytokine production in the kidney (36). Mice pre-treated with β-HB had lower nuclear factor kappa-light-chain-enhancer of activated B cells (NF-κB) activation, fewer infiltrating macrophages, and reduced caspase-3 cleavage in kidney tissue compared to untreated septic controls (36). These findings suggest ketone bodies act as epigenetic and anti-inflammatory mediators that improve cellular resilience during AKI.

Ketogenic metabolic interventions in animal models further support a beneficial role. Short-term KD or fasting has been shown to increase tolerance to ischemic AKI. In rats, as little as 2–3 days of a ketogenic regimen prior to renal ischemia markedly reduced tubular injury and oxidative damage, with improvements in post-ischemia kidney function (35). KD therapy also appears to blunt the chronic consequences of AKI. In a unilateral ureteral obstruction model of renal fibrosis, KD feeding attenuated tubulointerstitial fibrosis, an effect traced to enhanced FAO in renal tubules via the free fatty acid receptor 3 signaling pathway (35).

Restoration of FAO through KD was associated with lower macrophage infiltration and collagen deposition, indicating that ketosis can counteract the pro-fibrotic, maladaptive repair processes after injury (23). Likewise, a recent study reported that a ketogenic diet per se upregulated PPARα-driven FAO in the kidney and thereby suppressed fibrogenic pathways in post-AKI progression (23). Together, these studies highlight that KD shifts renal metabolism toward a more oxidative, fatty-acid fueled state, which can protect against AKI and improve recovery. This aligns with the concept that reprogramming metabolism (via diet or pharmacologic ketone supplements) may correct the energy imbalance in AKI – replenishing ATP, reducing oxidative stress, and modulating inflammatory signaling. Such insights provide a strong rationale for considering ketogenic interventions as an adjunct in managing AKI or its chronic sequelae, though clinical translation will require careful evaluation of safety and patient selection.

The strengths of this work lie in both its novelty and methodological depth. To our knowledge, this is the first experimental study to apply KD intervention in a SA-AKI model, addressing a major gap in metabolic therapy research for SA-AKI. Importantly, this study combines a comprehensive multi-omics approach with mechanistic validation through qPCR, Western blotting, and immunofluorescence analysis of key FAO regulators. This hybrid strategy ensures not only systems-level discovery but also molecular confirmation, enhancing the credibility of the findings. This integration of unbiased omics with focused validation exemplifies methodological rigor and provides a more complete picture of metabolic reprogramming in SA-AKI.

Nevertheless, some limitations should be acknowledged. While we confirmed the involvement of key FAO components at both mRNA and protein levels, functional causality remains to be established, as no targeted perturbation experiments (e.g., knockdown, pharmacologic inhibition) were conducted. Without such loss- or gain-of-function approaches, it is difficult to definitively prove that restoration of FAO is the sole driver of the observed renoprotective effects. In addition, our study primarily focused on the AMPK–PGC1α–PPARα signaling pathway, yet ketogenic interventions are known to exert broader biological effects. For example, β-HB not only serves as an alternative energy substrate but also functions as a signaling molecule with anti-inflammatory, antioxidative, and epigenetic properties, including inhibition of histone deacetylases and modulation of NF-κB activity (35, 36). These additional pathways may have contributed to the observed benefits and warrant further mechanistic exploration. Moreover, the study was performed in a single preclinical murine model, which may not fully recapitulate the clinical heterogeneity of SA-AKI. The relatively short intervention window also precludes evaluation of long-term consequences, such as progression to fibrosis or chronic kidney disease. Finally, the translational applicability of KD in critically ill patients remains uncertain, as strict dietary adherence, metabolic tolerance, and safety profiles need to be carefully assessed in the clinical context. Future investigations should therefore include targeted perturbation experiments to establish functional causality, validation in multiple SA-AKI models and clinical samples, and systematic evaluation of both FAO-dependent and FAO-independent mechanisms of KD. These efforts will help clarify whether KD can be developed into a feasible and effective metabolic therapy for SA-AKI.

5. Conclusions

In summary, this study provides a comprehensive characterization of how KD modulates renal metabolism in SA-AKI. By integrating multi-omics profiling with targeted validation, we identified a distinct metabolic phenotype marked by enhanced FAO and lipid remodeling. Mechanistic experiments further confirmed activation of classical FAO pathways under KD intervention. Together, these findings suggest that KD promotes renal FAO and offers a promising therapeutic strategy for SA-AKI. This integrative approach lays a solid foundation for future mechanistic and translational research on metabolic interventions in critical illness.

Data Availability Statement

The raw data supporting the conclusions of this article will be made available by the authors on request.

Ethical statements

This study involves animal models, all animal experimental protocols were reviewed and approved by the Institutional Animal Care and Use Committee of Harbin Medical University (SYDW2024-127).

Acknowledgements

We are grateful for the support provided by the Department of Critical Care Medicine at both the First and Second Affiliated Hospitals of Harbin Medical University for this study.

Appendix A. Supplementary data

Supplementary Methods 1: Detailed protocols for untargeted proteomics, PRM, untargeted metabolomics, and untargeted lipidomics.

Funding

The National Key Research and Development Program of China (Nos. 2021YFC2501800), National Natural Science Foundation of China (No.82472184), The Outstanding Youth Project of Heilongjiang Natural Science Foundation (Nos. JQ2021H002), Key R&D Plan Project in Heilongjiang Province (No. GY2023ZB0075), Harbin Medical University Foundation Youth Project (No. PYQN2023-9), Wu Jieping Medical Foundation (No.320.6750.2021-4-60), Research Project of Heilongjiang Provincial Health Commission (No.20241717010028). These funding bodies provided financial support for the design of the study, implementation of the animal experiments, and the analysis and interpretation of the multi-omics data.

References

1. Zarbock A, Nadim MK, Pickkers P, Gomez H, Bell S, Joannidis M, et al. Sepsis-associated acute kidney injury: consensus report of the 28th Acute Disease Quality Initiative workgroup. Nature Reviews Nephrology. 2023;19(6):401-17.
2. Song MJ, Jang Y, Legrand M, Park S, Ko R, Suh GY, et al. Epidemiology of sepsis-associated acute kidney injury in critically ill patients: a multicenter, prospective, observational cohort study in South Korea. Crit Care. 2024;28(1):383.
3. Li Y, Li H, Zhang D. Timing of continuous renal replacement therapy in patients with septic AKI. Medicine. 2019;98(33):e16800.

4. Toro J, Manrique-Caballero CL, Gómez H. Metabolic Reprogramming and Host Tolerance: A Novel Concept to Understand Sepsis-Associated AKI. Journal of Clinical Medicine. 2021;10(18).
5. Zhou Y, Zhou F, Wang X, Chang P, Zhang L, Yao Q, et al. Practice of Extracorporeal Therapies for Septic Acute Kidney Injury Patients in Intensive Care Units in Mainland China. Blood Purification. 2019;47(Suppl. 3):23-8.
6. Manrique-Caballero CL, Del Rio-Pertuz G, Gomez H. Sepsis-Associated Acute Kidney Injury. Critical Care Clinics. 2021;37(2):279-301.
7. Douvris A, Malhi G, Hiremath S, McIntyre L, Silver SA, Bagshaw SM, et al. Interventions to prevent hemodynamic instability during renal replacement therapy in critically ill patients: a systematic review. Critical Care. 2018;22(1):41.
8. Liu A-B, Tan B, Yang P, Tian N, Li J-K, Wang S-C, et al. The role of inflammatory response and metabolic reprogramming in sepsis-associated acute kidney injury: mechanistic insights and therapeutic potential. Frontiers in Immunology. 2024;15:1487576.
9. Gómez H. Reprogramming Metabolism to Enhance Kidney Tolerance during Sepsis: The Role of Fatty Acid Oxidation, Aerobic Glycolysis, and Epithelial De-Differentiation. Nephron. 2023;147(1):31-4.
10. Zhao L, Hao Y, Tang S, Han X, Li R, Zhou X. Energy metabolic reprogramming regulates programmed cell death of renal tubular epithelial cells and might serve as a new therapeutic target for acute kidney injury. Frontiers in Cell and Developmental Biology. 2023;11:1276217.
11. Li ZL, Li XY, Zhou Y, Wang B, Lv LL, Liu BC. Renal tubular epithelial cells response to injury in acute kidney injury. EBioMedicine. 2024;107:105294.
12. Wang T, Huang Y, Zhang X, Zhang Y, Zhang X. Advances in metabolic reprogramming of renal tubular epithelial cells in sepsis-associated acute kidney injury. Front Physiol. 2024;15:1329644.
13. Gao Z, Chen X. Fatty Acid β-Oxidation in Kidney Diseases: Perspectives on Pathophysiological Mechanisms and Therapeutic Opportunities. Frontiers in Pharmacology. 2022;13:805281.
14. Chang L-Y, Chao Y-L, Chiu C-C, Chen P-L, Lin HYH. Mitochondrial Signaling, the Mechanisms of AKI-to-CKD Transition and Potential Treatment Targets. International Journal of Molecular Sciences. 2024;25(3).
15. Xu W, Zhu Y, Wang S, Liu J, Li H. From Adipose to Ailing Kidneys: The Role of Lipid Metabolism in Obesity-Related Chronic Kidney Disease. Antioxidants. 2024;13(12).
16. Fontecha-Barriuso M, Martin-Sanchez D, Martinez-Moreno J, Monsalve M, Ramos A, Sanchez-Niño M, et al. The Role of PGC-1α and Mitochondrial Biogenesis in Kidney Diseases. Biomolecules. 2020;10(2).
17. Clark AJ, Parikh SM. Targeting energy pathways in kidney disease: the roles of sirtuins, AMPK, and PGC1α. Kidney International. 2021;99(4):828-40.
18. Law SK, Au DCT. A review of medicine and food homology on traditional Chinese medicine as functional food. Food & Medicine Homology. 2025.
19. Liu Z, Zhou H, Meng X, Zhang Y, Yu B, Zhang S, et al. Review on bioactive compounds and mechanisms in Rehmannia glutinosa. Journal of Future Foods. 2025.
20. Ma S, Yang J, Tominaga T, Liu C, Suzuki K. A Low-Carbohydrate Ketogenic Diet and Treadmill Training Enhanced Fatty Acid Oxidation Capacity but Did Not Enhance Maximal Exercise Capacity in Mice. Nutrients. 2021;13(2).
21. Paoli A. The Influence of Physical Exercise, Ketogenic Diet, and Time-Restricted Eating on De Novo Lipogenesis: A Narrative Review. Nutrients. 2025;17(4).
22. Basolo A, Magno S, Santini F, Ceccarini G. Ketogenic Diet and Weight Loss: Is There an Effect on Energy Expenditure? Nutrients. 2022;14(9).
23. Qiu Y, Hu X, Xu C, Lu C, Cao R, Xie Y, et al. Ketogenic diet alleviates renal fibrosis in mice by enhancing fatty acid oxidation through the free fatty acid receptor 3 pathway. Front Nutr. 2023;10:1127845.
24. Zhu H, Bi D, Zhang Y, Kong C, Du J, Wu X, et al. Ketogenic diet for human diseases: the underlying mechanisms and potential for clinical implementations. Signal Transduct Target Ther. 2022;7(1):11.
25. Hasson D, Goldstein SL, Standage SW. The application of omic technologies to research in sepsis-associated acute kidney injury. Pediatr Nephrol. 2021;36(5):1075-86.

26. Qiao J, Cui L. Multi-Omics Techniques Make it Possible to Analyze Sepsis-Associated Acute Kidney Injury Comprehensively. Front Immunol. 2022;13:905601.
27. Zhou L, Li H, Hu J, Meng J, Lv H, Yang F, et al. Plasma oxidative lipidomics reveals signatures for sepsis-associated acute kidney injury. Clin Chim Acta. 2023;551:117616.
28. Tillander V, Alexson SEH, Cohen DE. Deactivating Fatty Acids: Acyl-CoA Thioesterase-Mediated Control of Lipid Metabolism. Trends Endocrinol Metab. 2017;28(7):473-84.
29. Gao J, Huang L, Zhang Y, Wei L, Yu Z, Xing Y, et al. Acute kidney injury through a metabolic lens: pathological reprogramming mechanisms and clinical translation potential. Front Physiol. 2025;16:1602865.
30. Feingold KR, Wang Y, Moser A, Shigenaga JK, Grunfeld C. LPS decreases fatty acid oxidation and nuclear hormone receptors in the kidney. Journal of Lipid Research. 2008;49(10):2179-87.
31. Iwaki T, Bennion BG, Stenson EK, Lynn JC, Otinga C, Djukovic D, et al. PPARαcontributes to protection against metabolic and inflammatory derangements associated with acute kidney injury in experimental sepsis. Physiological Reports. 2019;7(10):e14078.
32. Jin K, Ma Y, Manrique-Caballero CL, Li H, Emlet DR, Li S, et al. Activation of AMP-activated protein kinase during sepsis/inflammation improves survival by preserving cellular metabolic fitness. The FASEB Journal. 2020;34(5):7036-57.
33. Li J, He W, Wu Q, Qin Y, Luo C, Dai Z, et al. Ketogenic diets and beta-hydroxybutyrate in the prevention and treatment of diabetic kidney disease: current progress and future perspectives. BMC Nephrol. 2025;26(1):127.
34. Rojas-Morales P, Leon-Contreras JC, Sanchez-Tapia M, Silva-Palacios A, Cano-Martinez A, Gonzalez-Reyes S, et al. A ketogenic diet attenuates acute and chronic ischemic kidney injury and reduces markers of oxidative stress and inflammation. Life Sci. 2022;289:120227.
35. Tang W, Wei Q. The metabolic pathway regulation in kidney injury and repair. Front Physiol. 2023;14:1344271.
36. Kim MJ, Kim YS, Kim SR, Lee DW, Lee SB, Kim IY. beta-hydroxybutyrate ameliorates sepsis-induced acute kidney injury. Mol Biol Rep. 2023;50(11):8915-23.